nature physics

ARTICLES

PUBLISHED ONLINE: 17 AUGUST 2015 | DOI: 10.1038/NPHYS3437

Discovery of a Weyl fermion state with Fermi arcs in niobium arsenide

Su-Yang Xu[1,2†], Nasser Alidoust[1,2†], Ilya Belopolski[1,2†], Zhujun Yuan[3], Guang Bian[1], Tay-Rong Chang[1,4], Hao Zheng[1], Vladimir N. Strocov[5], Daniel S. Sanchez[1], Guoqing Chang[6,7], Chenglong Zhang[3], Daixiang Mou[8,9], Yun Wu[8,9], Lunan Huang[8,9], Chi-Cheng Lee[6,7], Shin-Ming Huang[6,7], BaoKai Wang[6,7,10], Arun Bansil[10], Horng-Tay Jeng[4,11], Titus Neupert[12], Adam Kaminski[8,9], Hsin Lin[6,7], Shuang Jia[3,13] and M. Zahid Hasan[1,2*]

Three types of fermions play a fundamental role in our understanding of nature: Dirac, Majorana and Weyl. Whereas Dirac fermions have been known for decades, the latter two have not been observed as any fundamental particle in high-energy physics, and have emerged as a much-sought-out treasure in condensed matter physics. A Weyl semimetal is a novel crystal whose low-energy electronic excitations behave as Weyl fermions. It has received worldwide interest and is believed to open the next era of condensed matter physics after graphene and three-dimensional topological insulators. However, experimental research has been held back because Weyl semimetals are extremely rare in nature. Here, we present the experimental discovery of the Weyl semimetal state in an inversion-symmetry-breaking single-crystalline solid, niobium arsenide (NbAs). Utilizing the combination of soft X-ray and ultraviolet photoemission spectroscopy, we systematically study both the surface and bulk electronic structure of NbAs. We experimentally observe both the Weyl cones in the bulk and the Fermi arcs on the surface of this system. Our ARPES data, in agreement with our theoretical band structure calculations, identify the Weyl semimetal state in NbAs, which provides a real platform to test the potential of Weyltronics.

Weyl semimetals have received significant attention in recent years because they extend the classification of topological phases beyond insulators, host exotic Fermi arc surface states, demonstrate unusual transport phenomena and provide an emergent condensed matter realization of Weyl fermions, which do not exist as fundamental particles in the standard model[1–21]. Such kind of topologically non-trivial semimetals are believed to open a new era in condensed matter physics. In contrast to topological insulators, where only the surface states are interesting, a Weyl semimetal features unusual band structure in the bulk and on the surface, leading to novel phenomena and potential applications. This opens up unparalleled research opportunities, where both bulk- and surface-sensitive experimental probes can measure the topological nature and detect quantum phenomena. In the bulk, a Weyl semimetal has a band structure with band crossings, Weyl nodes, which are associated with definite chiral charges. Unlike the two-dimensional Dirac points in graphene, the surface-state Dirac point of a three-dimensional topological insulator or the three-dimensional Dirac points in the bulk of a Dirac semimetal, the degeneracy associated with a Weyl node does not require any symmetry for its protection, other than the translation symmetry of the crystal lattice. The low-energy quasiparticle excitations of a Weyl semimetal are chiral fermions described by the Weyl equation, well known in high-energy physics, which gives rise to a condensed matter analogue of the chiral anomaly associated with a negative magnetoresistance in transport[16–21]. On the surface, the non-trivial topology guarantees the existence of surface states in the form of 'Fermi arcs', which are open curves that connect the projections of the bulk Weyl nodes on the surface. These Fermi arcs are by themselves of great interest, because Fermi surfaces have to be closed contours in any purely two-dimensional band structure. They are further interesting because they lead to novel spin polarization textures[22], unusual quantum interference effects in tunnelling spectroscopies[23], and a new type of quantum oscillation[24], where electrons move in real space between different surfaces of a bulk sample when executing a constant-energy orbit in momentum space under an external magnetic field.

Despite the tremendous interest in Weyl semimetals, experimental research devoted to their discovery has been held back owing to their rareness in nature. The transition metal monoarsenides have recently been suggested as Weyl

[1]Laboratory for Topological Quantum Matter and Spectroscopy (B7), Department of Physics, Princeton University, Princeton, New Jersey 08544, USA. [2]Princeton Center for Complex Materials, Princeton Institute for Science and Technology of Materials, Princeton University, Princeton, New Jersey 08544, USA. [3]International Center for Quantum Materials, School of Physics, Peking University, Beijing 100871, China. [4]Department of Physics, National Tsing Hua University, Hsinchu 30013, Taiwan. [5]Paul Scherrer Institute, Swiss Light Source, CH-5232 Villigen PSI, Switzerland. [6]Centre for Advanced 2D Materials and Graphene Research Centre National University of Singapore, 6 Science Drive 2, Singapore 117546, Singapore. [7]Department of Physics, National University of Singapore, 2 Science Drive 3, Singapore 117542, Singapore. [8]Division of Materials Science and Engineering, Ames Laboratory, US DOE, Ames, Iowa 50011, USA. [9]Department of Physics and Astronomy, Iowa State University, Ames, Iowa 50011, USA. [10]Department of Physics, Northeastern University, Boston, Massachusetts 02115, USA. [11]Institute of Physics, Academia Sinica, Taipei 11529, Taiwan. [12]Princeton Center for Theoretical Science, Princeton University, Princeton, New Jersey 08544, USA. [13]Collaborative Innovation Center of Quantum Matter, Beijing 100871, China. †These authors contributed equally to this work. *e-mail: mzhasan@princeton.edu

semimetals[25–28]. However, the experimental demonstration of a Weyl semimetal state requires one to simultaneously probe the bulk and the surface topological characters of a sample. Here, we report the experimental discovery of the Weyl semimetal state in the inversion-symmetry-breaking single-crystalline compound NbAs. By combining low-energy (vacuum ultraviolet) and soft X-ray (SX) angle-resolved photoemission spectroscopies (ARPES), we directly observe both the Weyl cones in the bulk and the Fermi arc surface states on the (001) cleaving surface of NbAs. Specifically, our SX-ARPES data clearly reveals that the bulk bands touch at discrete points in the bulk Brillouin zone (BZ) and disperse linearly along both the in-plane and out-of-plane directions, which, therefore, form the Weyl cones. Our low-energy ARPES measurements reveal the existence of Fermi arc surface states and show that they connect the projected bulk Weyl nodes. Our systematic ARPES data, and its excellent agreement with our first-principles band structure calculations, collectively demonstrate the Weyl semimetal state in NbAs. Our discovery not only paves the way for the many fascinating topological quantum phenomena predicted in the Weyl semimetal state[17–22], but also establishes a new keystone in the correspondence and synergy between high-energy and condensed matter physics.

The crystal structure and theoretical considerations

Niobium arsenide, NbAs, crystallizes in a body-centred tetragonal Bravais lattice, space group $I4_1md$ (109), point group C_{4v}. Our X-ray diffraction (XRD) obtains lattice constants of $a = 3.45$ Å and $c = 11.68$ Å, consistent with two earlier crystallographic studies[29,30]. The basis consists of two Nb atoms and two As atoms (Fig. 1a). The lattice can be understood as a stack of square lattice layers, where each layer consists entirely of either Nb or As atoms. In the crystal, each layer is shifted by half a lattice constant in either the x or y direction relative to the layer below it. These shifts give the lattice a screw pattern along the z direction, which leads to a non-symmorphic C_4 rotation symmetry that requires a translation along the z direction by $c/4$, or one-fourth a lattice constant in the conventional unit cell. More importantly, it can be seen that the NbAs crystal lacks space inversion symmetry. As the system respects time-reversal symmetry, the broken inversion symmetry is a crucial condition, without which the Weyl semimetal phase is not possible. Figure 1b shows a scanning tunnelling microscope image on the cleaved (001) surface. The topography image clearly resolves a square lattice without any obvious defect, demonstrating the high quality of our sample. From the topography, we obtain a lattice constant $a = 3.49$ Å, consistent with the value determined by XRD.

We present an overview of the band structure of NbAs. Figure 1c shows the calculated band structure without spin–orbit coupling. It can be seen that the conduction and valence bands cross each other near the Σ, Σ′ and N points, in agreement with the semimetal ground state. Without spin–orbit coupling, the conduction and valence bands interpenetrate each other, giving rise to four 1D ring-like crossings at the $k_x = 0$ and $k_y = 0$ planes (the left panel of Fig. 1d). On the inclusion of spin–orbit coupling (the left panel of Fig. 1d), the bands become gapped everywhere along the rings, but a number of point-like band crossings, the Weyl nodes, emerge in the vicinity of the rings away from the $k_x = 0$ and $k_y = 0$ planes. Our calculation shows that there are in total 24 Weyl nodes, which can be categorized into two groups. We name the 8 Weyl nodes that are located on the $k_z = 2\pi/c$ plane as W1, and the other 16 away from the $k_z = 2\pi/c$ plane as W2. We further study the projection of these Weyl nodes onto the (001) surface. All W1 Weyl nodes project as single Weyl nodes in the close vicinity of the surface BZ edge $\bar{X}$ and $\bar{Y}$ points. On the other hand, interestingly, each pair of W2 Weyl nodes with the same chiral charge are projected onto the same location on the (001) surface BZ. Therefore, there are eight projected W2 Weyl nodes with the projected chiral charge of ±2. The distribution of the projected Weyl nodes and their projected chiral charges are shown in the right panel of Fig. 1d. The theoretically calculated and ARPES (001) Fermi surface measured at the incident photon energy of 50 eV are shown in Fig. 1e, respectively. A good agreement is found between the ARPES and the calculation results. We discuss some general features of the Fermi surface before going into details. The surface BZ is found to be a square. Moreover, the momentum space distance between the surface BZ centre $\bar{\Gamma}$ and the edge $\bar{X}$ or $\bar{Y}$ is about 0.91 Å^{-1} in our ARPES data. These observations are in agreement with the tetragonal lattice ($a = b = 3.45$ Å) of NbAs and the lattice constant ($\pi/a = \pi/3.45 = 0.91$). Our ARPES data show that the dominant features in the Fermi surface are located near the surface BZ edge $\bar{X}$ and $\bar{Y}$ points and the midpoints between the $\bar{\Gamma}$–$\bar{X}$ and the $\bar{\Gamma}$–$\bar{Y}$ lines. Furthermore, it can be seen from our data that the Fermi surface violates the C_4 rotational symmetry, even though the surface BZ is a square. This is consistent with the crystal structure, where the rotational symmetry is implemented as a screw axis that sends the crystal back into itself after a C_4 rotation and a translation by $(0, a/2, c/4)$ along the rotation axis. As a result, the (001) surface breaks the rotational symmetry of the crystal and the Fermi surface does not need to respect the C_4 symmetry.

Bulk Weyl fermions and Weyl nodes

We now present our ARPES data to demonstrate the existence of the bulk Weyl cones and the surface Fermi arcs in NbAs. We have systematically studied the electronic structure of NbAs using both low-energy (vacuum ultraviolet, 35 eV–90 eV in our experiments) and SX (350–1,000 eV in our experiments) ARPES. We found that at the vacuum ultraviolet incident photon energies (for example, Fig. 1e), the surface states dominate the ARPES spectral weight, whereas the bulk bands are very weak. On the other hand, at SX energies the situation is reversed and, therefore, the bulk bands become predominant, which is consistent with the enhanced bulk sensitivity at the SX energies. Furthermore, due to the Heisenberg uncertainty principle, increasing the photoelectron mean free path results in concomitant sharpening of the intrinsic k_z definition[31].

We start by presenting the measurement of the bulk Weyl cones using SX-ARPES. Figure 2a shows the calculated k_z–k_x Fermi surface contour of the bulk bands at the $k_y = 0$ plane. The Fermi surface consists of identical contours in the proximity of the Σ and S points. We note that these contours arise from the 1D nodal line crossings at the $k_y = 0$ plane without spin–orbit coupling (Fig. 1d), which explains why their shape is very similar to the nodal line crossings. As discussed above in Fig. 1d, we do not expect to observe the Weyl nodes in Fig. 2a because all Weyl nodes are away from the $k_y = 0$ plane. Figure 2b shows the ARPES measured k_z–k_x Fermi surface over multiple BZs along the k_z direction. We find a good agreement between our ARPES data and the calculation. Furthermore, we emphasize that the clear dispersion along the k_z direction observed in Fig. 2b shows that our SX-ARPES primarily measures the bulk bands instead of the surface states. We choose an incident photon energy (that is, a k_z value) that corresponds to the W2 Weyl nodes. Figure 2d shows the ARPES measured k_x–k_y Fermi surface at the k_z value that corresponds to the W2 Weyl nodes using an incident photon energy of 651 eV. We compare the SX and low-energy Fermi surface (Figs 2d and 1e). Although they are measured on the same (001) surface of the same sample, the SX-ARPES Fermi surface contains only Fermi points and is C_4 symmetric, whereas the low-energy ARPES Fermi surface contains many pockets and violates the C_4 symmetry. This, again, provides compelling evidence that the SX-ARPES is sensitive to the bulk electronic structure whereas the low-energy ARPES signal is dominated by the surface states. We show the schematic of the Fermi surface at the k_z that corresponds to W2 nodes in Fig. 2e. Apart from the eight W2 Weyl nodes, there are additional trivial pockets along the k_x and k_y directions, which are denoted by the red circles. This is consistent

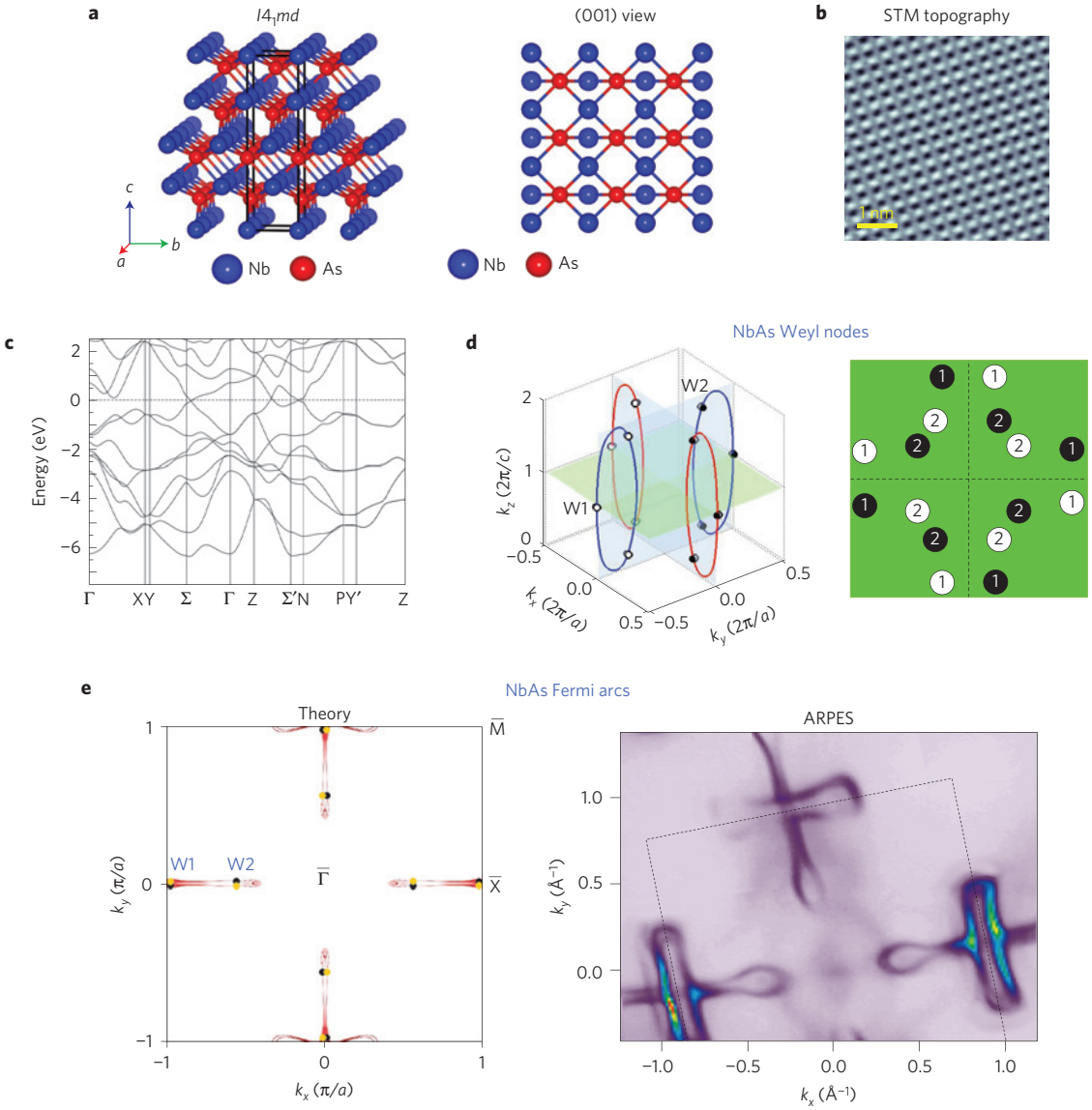

Figure 1 | Topological electronic structure of NbAs: Weyl nodes and Fermi arcs. a, Body-centred tetragonal structure of NbAs, shown as stacks of Nb and As layers. **b**, Scanning tunnelling microscopy (STM) topographic images of cleaved surfaces of NbAs used in our studies. **c**, First-principles band structure calculation of the bulk NbAs without spin–orbit coupling. **d**, (Left) Schematics of the distribution of the Weyl nodes in the three-dimensional Brillouin zone (BZ) of NbAs. The red and blue lines represent the nodal lines without considering spin–orbit coupling. (Right) Schematic cartoon (not to scale) showing the projected Weyl nodes and their chiral charges on the (001) Fermi surface of NbAs. The projected Weyl nodes are denoted by black and white circles whose colour indicates opposite chiral charges. **e**, First-principles band structure calculated (left) and the ARPES-measured Fermi surface (right) of the (001) Fermi surface of NbAs. The Fermi arcs are clearly resolved in our ARPES measurements in agreement with the theoretical prediction.

with our ARPES data in Fig. 2d. We therefore study the energy dispersion of the W2 Weyl cones by choosing a momentum space cut direction, Cut 1, which goes across a pair of W2 Weyl nodes, as noted in Fig. 2d. The dispersion map is shown in Fig. 2f over a wide energy range, where a linear dispersion is clearly observed. Because Cut 1 goes through two nearby W2 Weyl nodes, one would expect to observe two linearly dispersing cones in the ARPES spectra. However, the two cones are very close to each other in momentum space. According to our calculation, the k-space distance between the two W2 nodes is $0.024\pi/a \simeq 0.022$ Å^{-1}, which is challenging to resolve with SX-ARPES. However, owing to the sharp ARPES spectrum collected from our high-quality samples, we are able to barely see that the ARPES dispersion in Fig. 2g are consistent with the scenario with two cones. We further show a second derivative image of the dispersion in Fig. 2h, where the two cones are better seen. The k_y separation of the two Weyl nodes is about 0.025 Å^{-1}, which agrees with the calculation. As a Weyl cone features linear dispersion along all three directions, it is therefore also important to study the dispersion of the W2 Weyl bands along the out-of-plane k_z direction. We fix the k_x and k_y at the location that corresponds to a W2 Weyl node as shown by Cut 2 in Fig. 2d and study the energy dispersion as a function of k_z. As shown in Fig. 2i, the Weyl band is found to be strongly k_z-dispersive, which demonstrates its 3D nature. Moreover, throughout the k_z range shown in Fig. 2i, the band crosses the Fermi level only at two discrete k_z, where the k_z values of these two points are approximately $(52 \pm 1.2)\pi/c = \pm 1.2\pi/c$. This is again consistent with the k_z value of the W2 Weyl nodes from calculation, $k_z = \pm 1.16\pi/c$. In the vicinity of the two k_z values where the bands cross the Fermi level, the bands disperse linearly within our instrumental resolution (Fig. 2i). Our ARPES measured $E - k_z$ dispersion data in Fig. 2i is very consistent with the corresponding theoretical calculation in Fig. 2j.

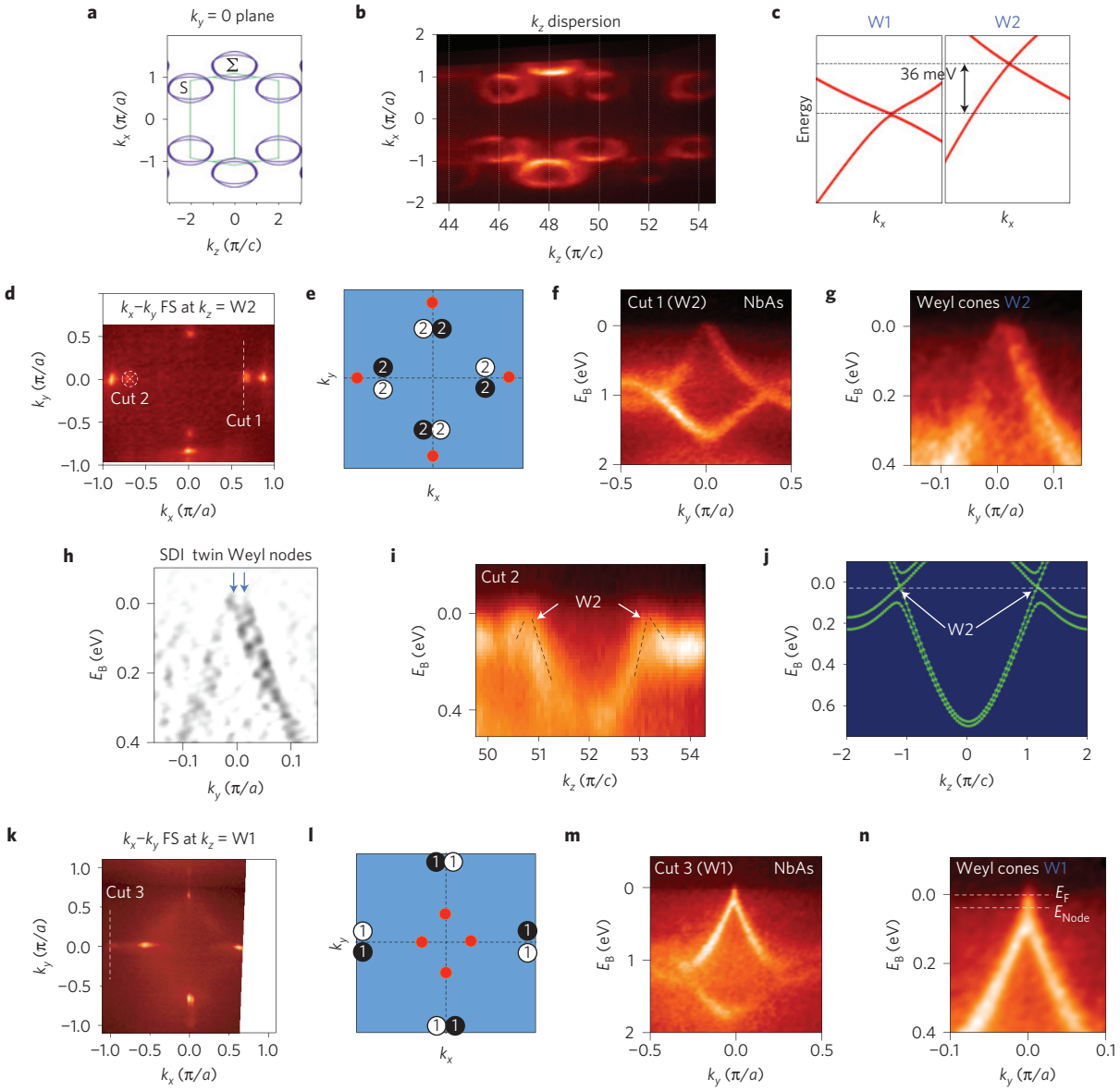

Figure 2 | Weyl cones in NbAs. a, First-principles calculated Fermi surface map at $k_y = 0$ in the k_z–k_x plane. **b**, Soft X-ray ARPES Fermi surface map at $k_y = 0$ in the k_z–k_x plane, which agrees well with the theoretical prediction in **a**. The measurements were conducted using photon energies ($\propto k_z$) of 518–800 eV. **c**, First-principles calculations of the energy–momentum dispersions of the two types of Weyl nodes (W1 and W2) in NbAs, which show that these nodes are offset in energy by 36 meV relative to each other. **d**, Soft X-ray ARPES Fermi surface map at $k_z = $ W2 in the k_x–k_y plane, revealing the locations of the W2 Weyl nodes. **e**, Schematics corresponding to **d** indicating the locations of the W2 Weyl nodes (black and white circles marked as '2') and other trivial bulk bands (red dots). **f**–**h**, Soft X-ray ARPES spectra (**f**), its zoomed-in version close to the Fermi level (**g**) and its curvature plot (**h**) along the Cut 1 direction shown in **d** that goes through the twin Weyl nodes marked as '2' in **e**. The photon energy of the measurements in **d**, **f** and **g** is 651 eV. **i**, Soft X-ray ARPES spectra along the Cut 2 direction shown in **d** (normal to the plane), which again reveals the existence of two Weyl cones along the k_z direction. **j**, First-principles calculations of the energy–momentum dispersions of the W2 Weyl nodes along k_z corresponding to the ARPES measurements in **i**. **k**, Soft X-ray ARPES Fermi surface map at $k_z = $ W1 in the k_x–k_y plane, revealing the locations of the W1 Weyl nodes. The photon energy here is 611 eV. **l**, Schematics corresponding to **k**, indicating the locations of the W1 Weyl nodes (black and white circles marked as '1') and other trivial bulk bands (red dots). **m**,**n** Soft X-ray ARPES spectra (**m**) and its zoomed-in version (**n**) close to the Fermi level along the Cut 3 direction shown in **k** that goes through the Weyl nodes marked as '1' in **l**. As can be seen in **n**, the energy of the W1 Weyl node is below the Fermi level and W2, in agreement with the calculations in **c**.

Figure 2k shows the k_x–k_y Fermi surface at the k_z value that corresponds to W1. The schematics of the expected Fermi surface at $k_z = $ W1 is shown in Fig. 2l. It can be seen that the Fermi surface at $k_z = $ W1 consists of both the W1 Weyl nodes that are very close to the surface BZ edge $[(k_x, k_y) = (\pi/a, 0)$ or $(0, \pi/a)]$ and some trivial pockets closer to the BZ centre. Therefore, we study the energy dispersion of the W1 Weyl cone by choosing a momentum space cut direction, Cut 3, as noted in Fig. 2k. We observe a clear dispersion of the W1 Weyl cone in Fig. 2m,n. Because Cut 3 goes across two nearby W1 Weyl nodes, one should, in principle, observe a pair of Weyl cones in the dispersion map depicted by Fig. 2m,n. However, because the two W1 Weyl nodes are extremely close to each other (the k-space separation is 0.007 Å^{-1} in our calculation, which is much smaller than in W2), our experimental resolution is not sufficient to resolve them. Moreover, our data shows that the W1 Weyl node is about 38 meV below the Fermi level and, as a result, a small part of the upper Weyl cone is seen. This is in agreement with the results from our first-principles calculation, shown in Fig. 2c.

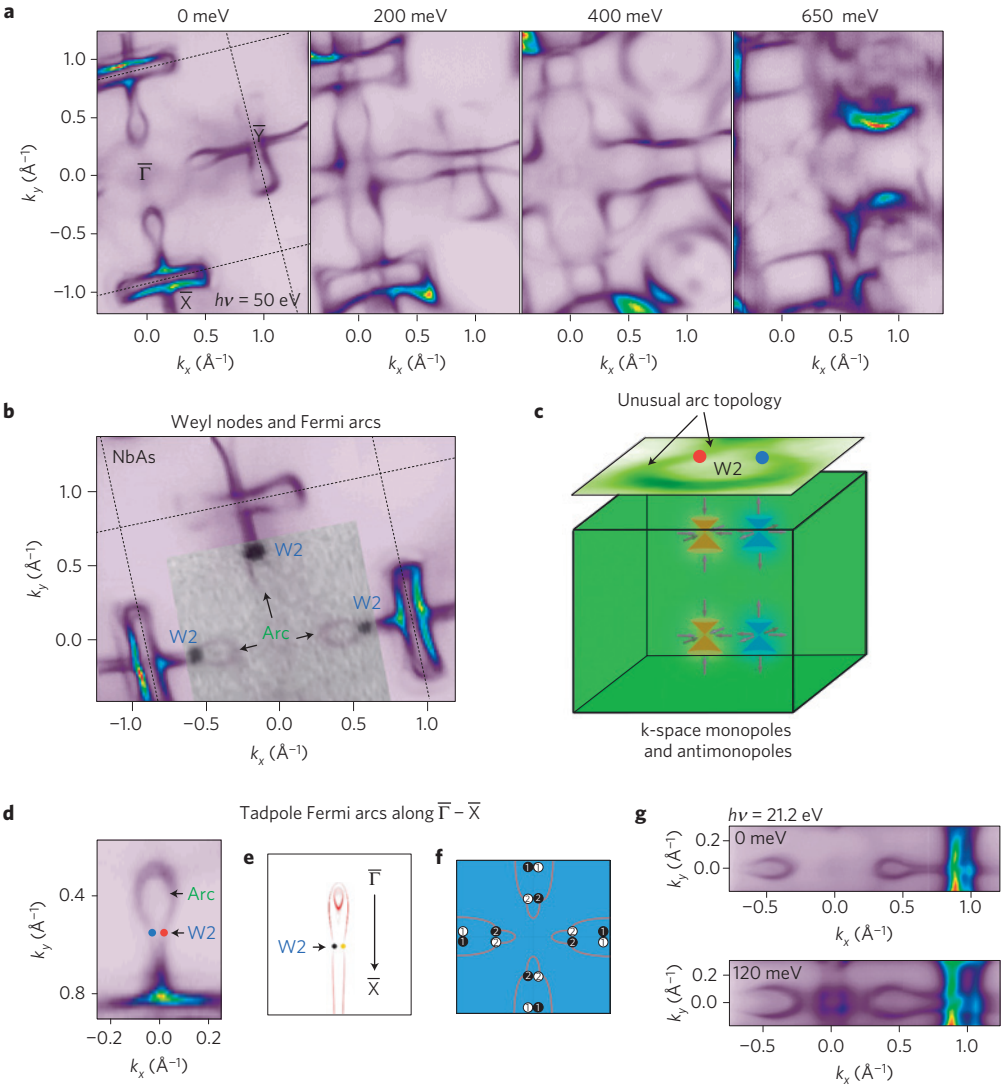

Figure 3 | Observation of Fermi arc surface states on the (001) surface of NbAs. a, High-resolution ARPES Fermi surface map and constant binding energy contours of the band structure of NbAs along the (001) direction at various energies. The square BZ and C_4 rotational symmetry at higher binding energies both clearly indicate that the sample is cleaved on the (001) surface. The C_4 violation by certain bands at shallow binding energies is consistent with C_4 screw axis symmetry broken by the (001) surface and clearly shows that the C_4 asymmetric states are surface states. **b**, High-resolution ARPES Fermi surface map, with the soft X-ray ARPES map from Fig. 2d overlaid on top of it to scale (greyscale region), showing the relative positions of the Fermi arcs and the Weyl nodes. **c**, Schematics of the locations of the W2 Weyl nodes in the bulk BZ of NbAs and the unusual topology of the Fermi arcs on the (001) surface Fermi surface in this compound. The pseudo-spin texture near the Weyl nodes with positive and negative chiral charges resembles the magnetic field around magnetic monopoles and antimonopoles. **d**, ARPES Fermi surface map of the tadpole Fermi arcs along $\bar{\Gamma}$–$\bar{X}$ and the corresponding Weyl nodes. **e**, First-principles calculated Fermi surface map of the tadpole Fermi arcs along $\bar{\Gamma}$–$\bar{X}$ which shows the qualitative agreement with the ARPES data. **f**, Schematics of the connectivity of the Fermi arcs in the first BZ. **g**, ARPES Fermi surface, and a constant binding energy contour at a binding energy of 120 meV, of the Fermi arcs along $\bar{\Gamma}$–$\bar{X}$.

Consequently, the systematic measurements presented here, when corroborated by our calculations, experimentally reveal the bulk Weyl cones in NbAs.

Surface Fermi arcs

After establishing the existence of the bulk Weyl cones, we study the Fermi arc surface states in NbAs by using low-energy (vacuum ultraviolet) ARPES in Fig. 3. Figure 3a shows the constant-energy contours of the (001) surface at different binding energies, with the incident photon energy fixed at 50 eV. At the Fermi level ($E_B = 0$ meV), our data shows that the Fermi surface consists of three dominant features: a dog-bone-shaped feature centred at the $\bar{Y}$ point, a long elliptical feature centred at the $\bar{X}$ point, and a tadpole-shaped feature that goes along either the $\bar{\Gamma}$–$\bar{X}$ or $\bar{\Gamma}$–$\bar{Y}$ line from the midpoint of the line towards the $\bar{X}$ ($\bar{Y}$) point. Our ARPES data and calculation (Fig. 1e) show agreement on the tadpole and the dog-bone surface states, but not on the elliptical feature. Note, the surface calculation result can be tuned by adjusting the surface potential and other surface parameters to further improve its consistency with the data. We focus on the tadpole surface states where the agreement between the data and the calculations is the best. As shown in Fig. 3d–g, the tadpole surface states give rise to the Fermi arcs that are connected to the W2 Weyl nodes. Specifically, the pair of W2 Weyl nodes are located at the joint between the 'head' and the 'tail' of the tadpole. Therefore, each W2 is connected to two Fermi arcs, consistent with its projected chiral charge of ±2, as illustrated in Fig. 3c. Because we have resolved both the W2 Weyl nodes using SX-ARPES (Fig. 2d) and the tadpole surface

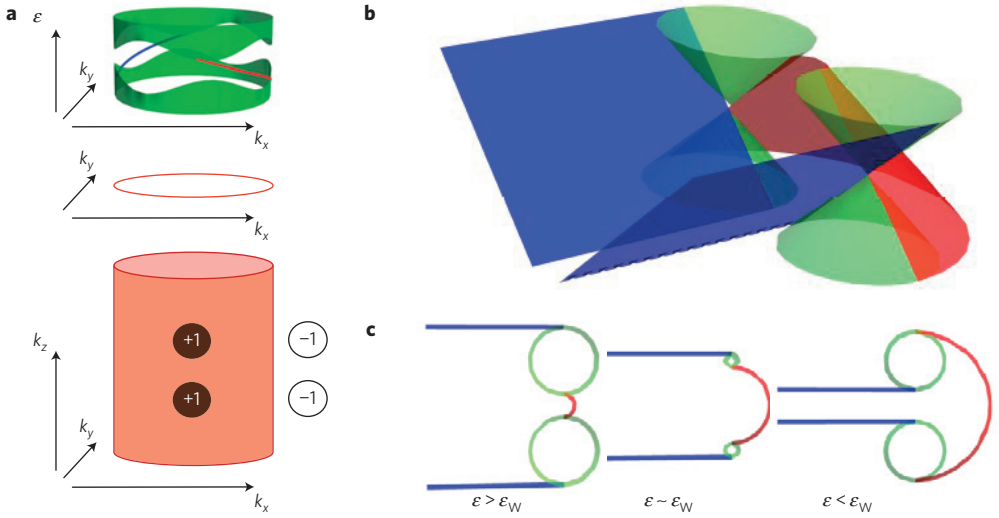

Figure 4 | Visualization of the co-propagating chiral modes and the structure of the tadpole Fermi arcs in NbAs. a, Bottom panel: a circular pipe through the bulk BZ of NbAs, enclosing two Weyl nodes of chiral charge +1. The pipe extends through the entire bulk BZ in the k_z direction, forming a closed manifold. Because it encloses two Weyl nodes of chiral charge +1, the Chern number on this manifold is +2. Middle panel: by cleaving an NbAs sample on the (001) surface, we introduce a boundary on this manifold corresponding to a circle in the surface BZ. Top panel: the Chern number of +2 requires that the band structure on this circle in the surface BZ have two gapless co-propagating chiral edge modes. **b**, Our direct experimental observation by ARPES of the way in which Fermi arcs connect Weyl nodes on the (001) surface of NbAs places strong constraints on the dispersion of the Fermi arcs. To be consistent with a chiral charge of ±2 for the projections of the Weyl nodes on the surface BZ, the tadpole Fermi arcs must disperse as shown by the red and blue sheets. The Weyl cones are shown in green. **c**, Constant-energy contours of the tadpole Fermi arc surface states at binding energies ε above the energy of the Weyl nodes ε_W, near the energy of the Weyl nodes and below the energy of the Weyl nodes. For the Fermi arcs to be co-propagating, the red sheet must grow with binding energy, whereas the blue sheets must disperse towards each other.

states using low-energy ARPES (Fig. 3a), we, therefore, superimpose these two Fermi surfaces together to scale, as shown in Fig. 3b. Indeed, we find that the W2 nodes are located between the 'head' and the 'tail' of the tadpole. This demonstrates that the observed tadpole surface states consist of three Fermi arcs, namely a curve that directly connects the pair of W2 nodes, and two nearly straight lines that runs from each W2 towards the surface BZ edge. On the other hand, resolving the Fermi arc connectivity associated with the W1 Weyl nodes is much more challenging, because the W1 nodes are too close to each other (the k-space separation is 0.007 $Å^{-1}$). We note that first-principles calculations of surface band structures are less reliable than that of the bulk, because surface calculations have additional free parameters (surface relaxation, surface density, on-site energies of surface atoms, and so on) that are difficult to predict. Specifically, topological theory requires that the number of Fermi arcs terminated onto a projected Weyl node must equal the magnitude of the projected chiral charge. But the details of the connectivity and the shapes of the Fermi arcs in surface calculations depend on these free parameters mentioned above. Therefore, the consistency between theory and experiments over the elliptical feature at the $\bar{Y}$ point can be improved by optimizing these free parameters in theory. We emphasize that our observation of the tadpole Fermi arc surface states that connect the W2 Weyl nodes is sufficient to experimentally establish the existence of Fermi arc surface states in NbAs.

Discussions

We elaborate the key distinctions between the two prototypical Weyl semimetals NbAs and TaAs. We first note their common properties: both are Weyl semimetals and both feature 24 Weyl nodes in the bulk according to band calculations[25]. There is an energy offset between the W1 and the W2 Weyl nodes, meaning that it is not possible to find an energy where the bulk density of states vanishes. Therefore, to achieve any surface transport that arises from the Fermi arcs[24], a sufficiently large external magnetic field is needed to gap out the bulk carriers. On the (001) surface of both materials, the 24 Weyl nodes form 16 projected Weyl nodes. 8 of them (W1) have projected chiral charge of ±1 and the other 8 (W2) have projected chiral charge of ±2. On the other hand, these two Weyl semimetals also have important differences both in the bulk and on the surface. In the bulk, the k-space splittings between the Weyl nodes in TaAs is about three times larger than those of in NbAs, revealing the fact that the Weyl nodes arise from spin–orbit coupling. On the (001) surface, our ARPES data reveal a new form of Fermi arc (connectivity) in NbAs, which is distinct from TaAs. In TaAs, we found that the two nearby projected W2 nodes are directly connected to each other by two Fermi arcs, which take the shape of a crescent[27]. By contrast, in NbAs, our data and calculations (Fig. 3) show that one Fermi arc, the head of the tadpole, directly connects the two projected W2 nodes, whereas the other Fermi arc, the tail of the tadpole, goes from a projected W2 node towards the surface BZ boundary. As mentioned in the previous paragraph, the pattern of connectivity of the Fermi arcs can vary depending on material details. The observed different Fermi arc connectivity patterns in NbAs and TaAs provide an experimental example of both the constraints imposed and the freedoms allowed to the Fermi arc electronic structure by the non-trivial topology in a Weyl semimetal. The novel Fermi arc connectivity is further important as it plays an essential role in the surface transport and surface quasiparticle interference experiments. It would be interesting to study the evolution of the surface Fermi arcs and their connectivity in $Nb_{1-x}Ta_xAs$.

Our direct experimental observation by ARPES of the unusual way in which Fermi arcs connect projected Weyl nodes on the (001) surface of NbAs places strong constraints on the dispersion of the Fermi arcs. To understand how, we recall first that the Weyl nodes W2 are arranged in such a way that, for an NbAs sample cleaved on the (001) surface, two Weyl nodes of the same chirality project onto the same point of the surface BZ. As a result, each of the Weyl node projections has a chiral charge of ±2. This chirality requires not only that two Fermi arcs connect to each of the Weyl

node projections in the surface BZ, but also that the Fermi arcs connecting to a given Weyl node projection be co-propagating. To clarify this requirement, consider a circular pipe passing through the bulk BZ of NbAs which encloses two Weyl nodes of chiral charge +1 (refs 5,8,10), as shown in the bottom panel of Fig. 4a. The Chern number on this manifold, a 2D effective Chern insulator, is +2. By cleaving the NbAs sample on the (001) surface, we introduce a boundary on this manifold corresponding to a circle in the surface BZ, as shown in the middle panel of Fig. 4a. On this circle, the Chern number of +2 requires that the band structure have two gapless co-propagating chiral boundary modes, illustrated by the red and blue curves in the top panel of Fig. 4a. By determining the chirality of the Fermi arc surface states using this circle in the surface BZ, we see that if the Weyl nodes are connected by tadpole Fermi arcs, as we observe in our ARPES spectra, then the Fermi arcs must disperse as illustrated in Fig. 4b. The green cones correspond to the Weyl cones projected onto the surface BZ, whereas the red and blue sheets correspond to the tadpole Fermi arcs. We can better visualize the evolution as a function of binding energy by considering cuts through this band structure. In Fig. 4c, we illustrate constant-energy contours of this band structure at a cut above the energy of the Weyl nodes $\varepsilon > \varepsilon_W$, near the energy of the Weyl nodes $\varepsilon \sim \varepsilon_W$ and below the energy of the Weyl nodes $\varepsilon < \varepsilon_W$. We find that the condition for co-propagating chiral modes actually requires the red surface states to grow with binding energy, whereas the blue surface states shrink with binding energy. Our prediction of this structure of the tadpole Fermi arc surface states is consistent with our numerical calculation of the chiral charge of Weyl nodes in NbAs and our direct experimental observation by ARPES of the unusual way in which Fermi arcs connect Weyl nodes on the (001) surface of NbAs.

Methods

Methods and any associated references are available in the online version of the paper.

Received 21 May 2015; accepted 14 July 2015;
published online 17 August 2015

References

1. Pal, B. P. Dirac, Majorana and Weyl fermions. *Am. J. Phys.* **79,** 485–498 (2011).
2. Weyl, H. Elektron und gravitation. I. *Z. Phys.* **56,** 330–352 (1929).
3. Balents, L. Weyl electrons kiss. *Physics* **4,** 36 (2011).
4. Wilczek, F. Why are there analogies between condensed matter and particle theory? *Phys. Today* **51,** 11–13 (1998).
5. Turner, A. M. & Vishwanath, A. in *Topological Insulators* (eds Franzand, M. & Molenkamp, L.) (Elsevier, 2013).
6. Haldane, F. D. M. Attachment of surface "Fermi arcs" to the bulk Fermi surface: "Fermi-level plumbing" in topological metals. Preprint at http://arXiv.org/abs/1401.0529 (2014).
7. Hasan, M. Z., Xu, S.-Y. & Neupane, M. in *Topological Insulators: Fundamentals and Perspectives* (eds Ortmann, F., Roche, S. & Valenzuela, S. O.) 55–100 (John Wiley, 2015).
8. Wan, X., Turner, A. M., Vishwanath, A. & Savrasov, S. Y. Topological semimetal and Fermi-arc surface states in the electronic structure of pyrochlore iridates. *Phys. Rev. B* **83,** 205101 (2011).
9. Murakami, S. Phase transition between the quantum spin Hall and insulator phases in 3D: Emergence of a topological gapless phase. *New J. Phys.* **9,** 356 (2007).
10. Burkov, A. A. & Balents, L. Weyl semimetal in a topological insulator multilayer. *Phys. Rev. Lett.* **107,** 127205 (2011).
11. Xu, G. *et al.* Chern semi-metal and quantized anomalous Hall effect in $HgCr_2Se_4$. *Phys. Rev. Lett.* **107,** 186806 (2011).
12. Singh, B. *et al.* Topological electronic structure and Weyl semimetal in the $TlBiSe_2$ class of semiconductors. *Phys. Rev. B* **86,** 115208 (2012).
13. Bulmash, D., Liu, C.-X. & Qi, X.-L. Prediction of a Weyl semimetal in $Hg_{1-x-y}Cd_xMn_yTe$. *Phys. Rev. B* **89,** 081106(R) (2014).
14. Liu, J. & Vanderbilt, D. Weyl semimetals from noncentrosymmetric topological insulators. *Phys. Rev. B* **90,** 155316 (2014).
15. Xu, S.-Y. *et al.* Topological phase transition and texture inversion in a tunable topological insulator. *Science* **332,** 560–564 (2011).
16. Nielsen, H. B. & Ninomiya, M. The Adler–Bell–Jackiw anomaly and Weyl fermions in a crystal. *Phys. Lett. B* **130,** 389–396 (1983).
17. Zyuzin, A. A. & Burkov, A. A. Topological response in Weyl semimetals and the chiral anomaly. *Phys. Rev. B* **86,** 115133 (2012).
18. Wei, H., Chao, S.-P. & Aji, V. Excitonic phases from Weyl semimetals. *Phys. Rev. Lett.* **109,** 196403 (2012).
19. Parameswaran, S. A., Grover, T., Abanin, D. A., Pesin, D. A. & Vishwanath, A. Probing the chiral anomaly with nonlocal transport in three-dimensional topological semimetals. *Phys. Rev. X* **4,** 031035 (2014).
20. Ashby, P. E. C. & Carbotte, J. P. Magneto-optical conductivity of Weyl semimetals. *Phys. Rev. B* **87,** 245131 (2013).
21. Vazifeh, M. M. & Franz, M. Electromagnetic response of Weyl semimetals. *Phys. Rev. Lett.* **111,** 027201 (2013).
22. Ojanen, T. Helical Fermi arcs and surface states in time-reversal invariant Weyl semimetals. *Phys. Rev. B* **87,** 245112 (2013).
23. Hosur, P. Friedel oscillations due to Fermi arcs in Weyl semimetals. *Phys. Rev. B* **86,** 195102 (2012).
24. Potter, A. C., Kimchi, I. & Vishwanath, A. Quantum oscillations from surface Fermi-arcs in Weyl and Dirac semi-metals. *Nature Commun.* **5,** 5161 (2014).
25. Huang, S.-M. *et al.* An inversion breaking Weyl semimetal state in the TaAs material class. *Nature Commun.* **6,** 7373 (2015).
26. Weng, H., Fang, C., Fang, Z., Bernevig, A. & Dai, X. Weyl semimetal phase in non-centrosymmetric transition metal monophosphides. *Phys. Rev. X* **5,** 011029 (2015).
27. Xu, S. Y. *et al.* Discovery of a Weyl Fermion semimetal and topological Fermi arcs. *Science* http://dx.doi.org/10.1126/science.aaa9297 (2015).
28. Lv, B. Q. *et al.* Discovery of Weyl semimetal TaAs. Preprint at http://arXiv.org/abs/1502.04684 (2015).
29. Furuseth, S. & Kjekshuh, A. The crystal structure of NbAs. *Acta Crystallogr.* **17,** 1077–1078 (1964).
30. Boller, H. & Parthe, E. The transposition structure of NbAs and of similar monophosphides and arsenides of niobium and tantalum. *Acta Crystallogr.* **16,** 1095–1101 (1963).
31. Strocov, V. N. *et al.* Soft-X-ray ARPES facility at the ADRESS beamline of the SLS: Concepts, technical realisation and scientific applications. *J. Synchrotron Radiat.* **21,** 32–44 (2014).

Acknowledgements

Work at Princeton University and Princeton-led synchrotron-based ARPES measurements were supported by the Gordon and Betty Moore Foundations EPiQS Initiative through Grant GBMF4547 (M.Z.H.). First-principles band structure calculations at National University of Singapore were supported by the National Research Foundation, Prime Minister's Office, Singapore under its NRF fellowship (NRF Award No. NRF-NRFF2013-03). Single-crystal growth was supported by National Basic Research Program of China (Grant Nos. 2013CB921901 and 2014CB239302) and by DE-FG-02-05ER46200. T.-R.C. and H.-T.J. were supported by the National Science Council, Taiwan. H.-T.J. also thanks National Center for High-Performance Computing (NCHC), Computer and Information Network Center National Taiwan University (CINC-NTU), and National Center for Theoretical Sciences (NCTS), Taiwan, for technical support. L.H. is supported by CEM, an NSF MRSEC, under grant DMR-1420451. Experiments at the Ames Laboratory in the Iowa State University were supported by the US Department of Energy, Office of Basic Energy Sciences, Division of Materials Sciences and Engineering under Contract No. DE-AC02-07CH11358. The work at Northeastern University was supported by the US Department of Energy (DOE), Office of Science, Basic Energy Sciences grant number DE-FG02-07ER46352, and benefited from Northeastern University's Advanced Scientific Computation Center (ASCC) and the NERSC Supercomputing Center through DOE grant number DE-AC02-05CH11231. We gratefully thank S.-k. Mo, J. Denlinger, A. V. Fedorov, M. Hashimoto, M. Hoesch and T. Kim for their beamline assistance at the Advanced Light Source, the Stanford Synchrotron Radiation Lightsource and the Diamond Light Source. We thank D. Huse, I. Klebanov, A. Polyakov, P. Steinhardt, H. Verlinde and A. Vishwanath for discussions. T.-R.C. and H.L. acknowledge visiting scientist support from Princeton University. We also thank C.-H. Hsu for technical assistance in the theoretical calculations.

Author contributions

S.-Y.X., N.A., I.B., G.B. and D.S.S. conducted the ARPES experiments with assistance from H.Z., V.N.S., D.M., Y.W., L.H., A.K. and M.Z.H.; Z.Y., C.Z. and S.J. grew the single-crystal samples; H.Z. conducted the STM measurements with assistance from G.B., S.-Y.X. and D.S.S.; T.-R.C., G.C., C.-C.L., S.-M.H., B.W., A.B., H.-T.J. and H.L. performed first-principles band structure calculations; T.N. did theoretical analyses; M.Z.H. was responsible for the overall direction, planning and integration among different research units.

Additional information

Reprints and permissions information is available online at www.nature.com/reprints. Correspondence and requests for materials should be addressed to M.Z.H.

Competing financial interests

The authors declare no competing financial interests.

Methods

High-quality single crystals of NbAs were grown by the standard chemical vapour transport method[29,30]. High-resolution vacuum ultraviolet angle-resolved photoemission spectroscopy (ARPES) measurements were performed using ARPES instruments based at the synchrotron-radiation light sources at Beamlines 4.0.3, 10.0.1 and 12.0.1 of the Advanced Light Source (ALS) at the Lawrence Berkeley National Laboratory (LBNL), Beamline 5-4 of the Stanford Synchrotron Radiation Light source (SSRL) at the Stanford Linear Accelerator Center (SLAC), Beamline I05 of the Diamond Light Source (DLS), with an incident photon energy ranging from 15 to 100 eV, and using the home-built ARPES instrument at the Ames Laboratory in Ames, Iowa, equipped with an unpolarized He-Iα light (21.2 eV). The energy and momentum resolution of the vacuum ultraviolet ARPES instruments was better than 30 meV and 1% of the surface Brillouin zone, respectively. Samples were cleaved *in situ* under a vacuum condition better than 5×10^{-11} torr. The SX-ARPES measurements were performed at the ADRESS Beamline at the Swiss Light Source in the Paul Scherrer Institut (PSI). The experimental geometry of SX-ARPES has been described in ref. 31. The sample was cooled down to 12 K to quench the electron–phonon interaction effects reducing the k-resolved spectral fraction. The SX photon energy ranged from 300 to 1,000 eV. The combined (beamline and analyser) experimental energy resolution of the SX-ARPES varied between 40 and 80 meV. The angular resolution of the SX-ARPES analyser was 0.07°. First-principles calculations were performed by the OPENMX code based on norm-conserving pseudo-potentials generated with multi-reference energies and optimized pseudoatomic basis functions within the framework of the generalized gradient approximation (GGA) of density functional theory (DFT; ref. 32). Spin–orbit coupling was incorporated through j-dependent pseudo-potentials. For each Nb atom, three, two, two and one optimized radial functions were allocated for the s, p, d and f orbitals ($s3p2d2f1$), respectively, with a cutoff radius of 7 Bohr. For each As atom, $s3p3d3f2$ was adopted with a cutoff radius of 9 Bohr. A regular mesh of 1,000 Ry in real space was used for the numerical integrations and for the solution of the Poisson equation. A k-point mesh of $17 \times 17 \times 5$ for the conventional unit cell was used and experimental lattice parameters[29] were adopted in the calculations. Symmetry-respecting Wannier functions for the As p and Nb d orbitals were constructed without performing the procedure for maximizing localization and a real-space tight-binding Hamiltonian was obtained[33]. This Wannier-function-based tight-binding model was used to obtain the surface states by constructing a slab with a thickness of 80 atomic layers with Nb on the top and As on the bottom.

References

32. Perdew, J. P., Burke, K. & Ernzerhof, M. Generalized gradient approximation made simple. *Phys. Rev. Lett.* **77,** 3865–3868 (1996).
33. Weng, H., Ozaki, T. & Terakura, K. Revisiting magnetic coupling in transition-metal-benzene complexes with maximally localized Wannier functions. *Phys. Rev. B* **79,** 235118 (2009).